

EVALUATING INSTALLATION EFFECTS IN SEMI-SPAN WIND TUNNEL EXPERIMENTS USING CARTESIAN-GRID-BASED FLOW SOLVER UTCART

Yoshiharu Tamaki¹, Yuto Yokoyama¹, Taro Imamura¹

¹The University of Tokyo, 7-3-1 Hongo, Tokyo, Japan

Abstract

The model installation effects in the semi-span wind tunnel experiment on the stall characteristics of the CRM-HL are investigated through RANS-based CFD simulations. Multiple configurations with different boundary conditions for the wind tunnel floor or different peniche (i.e., the extension piece of the symmetry plane of the model) are simulated using the Cartesian-grid-based flow solver UTCart. The results suggest that the floor boundary layer thickens the boundary layer over the fuselage and promotes the flow separation at the wing root. Also, the peniche increases the effective angles of attack at the inboard sections and makes the flow prone to separation. Therefore, the flow separation tends to occur from the leading edge of the inboard wing when the peniche height is too high. Furthermore, the gap between the floor and the model decreases the effective angle of attack in the inboard region, contrary to the peniche.

Keywords: Aerodynamics, Wind-tunnel experiment, CFD, High-lift device, Stall

1. Introduction

Semi-span aircraft models have often been employed to maximize the Reynolds number in limited wind-tunnel facilities (e.g., [1, 2]). Such models are usually installed on the wind tunnel floor. Hence, the boundary layer developing over the wind tunnel floor may interfere with the installed model. The interference may be reduced by inserting an extended piece (usually called peniche or standoff) between the central line of the model and the wall. The peniche potentially has non-negligible aerodynamic effects, which introduce uncertainty in estimating the aircraft aerodynamics. Therefore, the height and shape of the peniche should be chosen carefully to compare the aerodynamics of the semi-span model and the actual aircraft.

Several existing studies [3-9] have addressed the aerodynamic effects of the peniche and floor boundary layer. For example, Gatlin and McGhee [3] conducted wind-tunnel experiments using full-span and semi-span models and evaluated the influences of the peniche height and floor boundary layer. They reported that the lift, drag, and lift slope obtained by the semi-span model experiment agree well with those obtained by the full-span model experiment when the peniche height is approximately equal to the floor boundary layer thickness. However, a substantial reduction of the stall angle was also observed in the semi-span model experiment. Yokokawa et al. [4] conducted computational fluid dynamics (CFD) simulations of a high-lift configuration with peniche and wind tunnel walls to determine the peniche height used in the wind tunnel experiment. They reported that the increase in the peniche height induces an increase in the effective aspect ratio and strengthens the suction peak at the high angles of attack. Also, Ito et al. [5] compared the free-air and in-tunnel configurations using CFD analysis. They showed that the floor boundary layer thickens the boundary layer over the fuselage and inboard wing. Such a thickened boundary layer promotes the flow separation at the wing root and may cause an earlier stall. Moreover, Eder et al. [6] and Skinner and Zare-Behtash [7] tested peniche-less configurations, where a gap is introduced between the model

and the floor. These studies showed that the obtained lift slope agrees better with the full-span model experiment than with a conventional peniche, and the results are less sensitive to the gap height. Nonetheless, the effects of the gap on stall behavior have been little addressed in these studies.

For a more precise understanding of the model installation effects, especially those on the stall behavior, we need to investigate the aerodynamics of multiple configurations with various peniche settings. CFD analysis seems suitable for this purpose, although simulating the many different configurations requires substantial effort for grid generation. In particular, the simulations of the intunnel geometry require re-meshing at each angle of attack, which significantly increases the turnaround time.

In this study, we extensively investigate the model installation effects on the aerodynamics of a high-lift configuration through CFD analysis to understand and enhance the validity of the semi-span wind tunnel experiments. For this purpose, we conduct CFD simulations based on the Reynolds-averaged Navier–Stokes (RANS) equation for multiple configurations with different peniche heights or those with a gap between the model and floor using the University Tokyo Cartesian-grid-based automatic flow solver (UTCart) [10, 11]. UTCart enables fully automatic grid generation using a tree-based algorithm and hence realizes rapid turn-around time in simulating the different configurations.

This paper is organized as follows. First, Section 2 summarizes the problem settings, including the geometry, computational grid, and simulation methodology. Then, Section 3 describes the validation of the present simulations, where the results are compared to the reference wind tunnel experiment [1]. Next, the effects of the peniche height and floor boundary layer are investigated in Section 4, and then, the configurations with a gap between the model and the floor are tested in Section 5. Finally, concluding remarks are provided in Section 6.

2. Problem settings

The target of the present CFD simulations is the flow around the high-lift common research model (CRM-HL), which was adopted as the test case of the 4th AIAA CFD High-Lift Prediction Workshop (HLPW-4) [12, 13]. For this model, the experimental data obtained by the QinetiQ 5m wind tunnel [1] and the geometry of the wind tunnel walls are available on the website [12]. In the following, the model geometry is described based on the original CRM-HL definition (i.e., the mean aerodynamic chord (MAC) $C_{\rm ref}$ =275.8 inch), although the experiment employed a 10% scale model. The simulation geometry contains a peniche (see Fig. 1). For reference, we also conduct simulations without the wind tunnel walls. In these simulations, the far-field boundary is set at $1024C_{\rm ref}$ away from the model, and a symmetry boundary condition is imposed at the half-cut plane (y = 0). In the following, the configurations with and without the wind tunnel wall are denoted as in-tunnel

and free-air configurations, respectively. For the in-tunnel configuration, the peniche height is changed from 0, 35, and 175 inches to investigate the effects of the peniche height. In addition, the influence of the floor boundary layer is evaluated by switching the tunnel wall boundary condition from nonslip to slip walls. Here, the case names are indicated by the combination of the peniche height and the tunnel wall boundary condition (i.e., nonslip (N) or slip (S)), as summarized in Table 1. Among these cases, 35N is the baseline case, i.e., the same setting as the wind tunnel experiment [1]. Furthermore, we also simulate two additional cases (35N-g1, 35N-g2), where a gap is introduced between the floor and the fuselage, as shown in Fig. 2.

Table 1 Case settings.

Table 1 Gade cettings.				
Case	Peniche height inch	Boundary condition for		
		the wind tunnel walls		
0S	0	Slip wall		
0N	0	Nonslip wall		
35S	35	Slip wall		
35N (baseline)	35	Nonslip wall		
175N	175	Nonslip wall		
35N-g1	0 (with 35-inch gap, see Fig. 2)	Nonslip wall		
35N-g2	17.5 (with 17.5-inch gap, see Fig. 2)	Nonslip wall		
FA	0	No tunnel walls		
		(free-air simulation with a symmetry BC)		

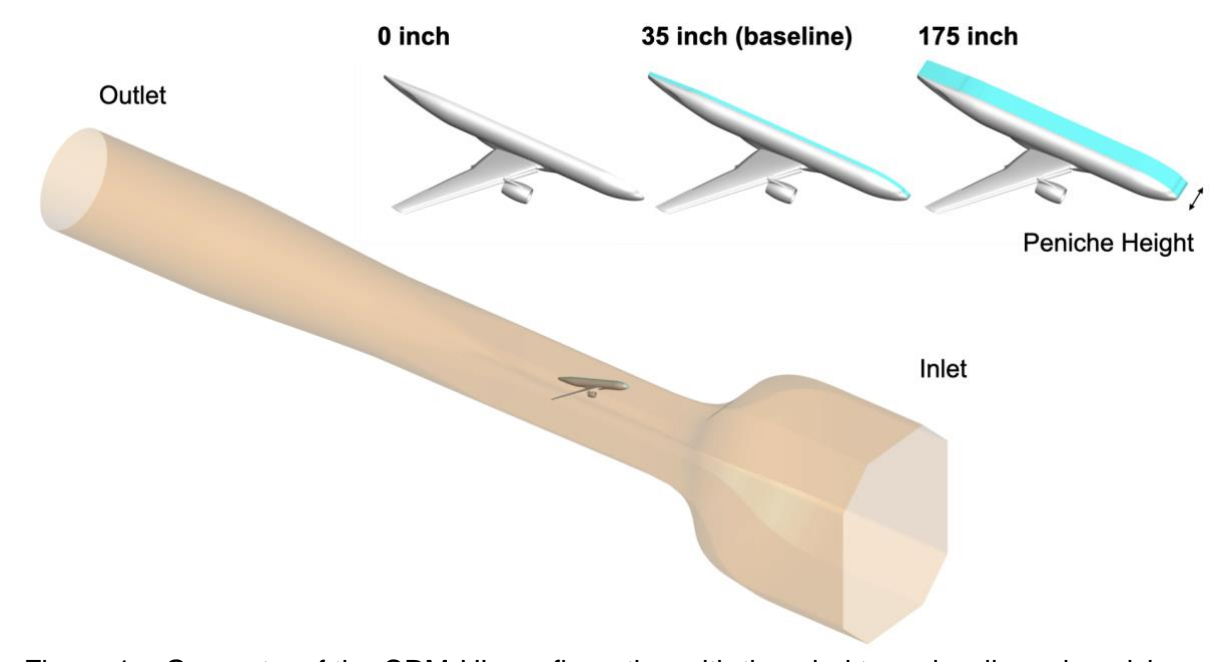


Figure 1 – Geometry of the CRM-HL configuration with the wind tunnel walls and peniche.

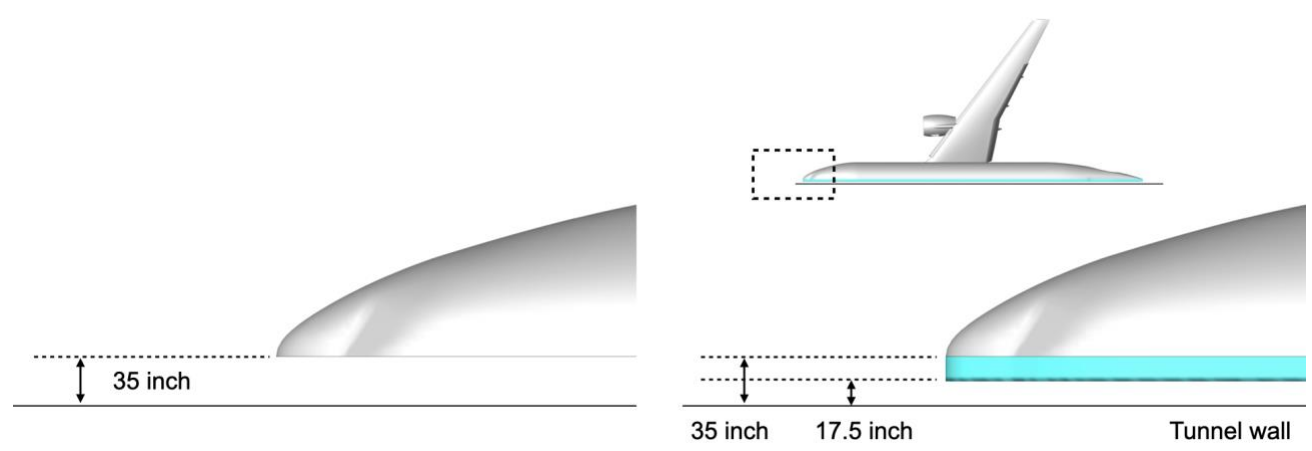


Figure 2 – Gaps between the wind-tunnel wall and fuselage (left: 35N-g1, right 35N-g2).

The flow conditions are adjusted to the reference wind tunnel experiment [1]. The Reynolds number based on the MAC and freestream velocity is 5.5×10^6 . For the free-air configuration, the freestream Mach number is set to 0.2. For the in-tunnel configurations, the total pressure and total temperature are specified at the inlet. At the outlet, the static pressure is adjusted so that the Mach number at the test section becomes within 0.195~0.205. For more detail on the boundary conditions for the intunnel configurations, see the problem definition of the HLPW-4 workshop website [12]. Note that all

the simulations are started from a cold-flow (i.e., freestream) condition.

For the in-tunnel configurations, the geometric angle of attack α is set to 1,99°, 5.98°, 15.48°, 17.98°, and 19.98°. These angles correspond to the tunnel-corrected angles of attack $\alpha_c = 2.78^\circ$, 7.05°, 17.05°, 19.57°, and 21.47°, respectively. For the free-air configuration, the geometric angles of attack are equal to these α_c values. The computations were parallelized using the message-passing interface with 768 CPU cores. The typical in-tunnel simulation case takes about 12 hours to achieve iterative convergence of the aerodynamic coefficients.

2.1 Simulation methodology

The present simulations employ UTCart [10,11]. UTCart consists of a hierarchical Cartesian grid generator and a compressible flow solver. The hierarchical Cartesian grid is generated based on a quadtree/octree-based algorithm. Hence, the overall workflow of UTCart is fully automatic.

A unique feature of UTCart is the immersed boundary method with a turbulent wall function [14]. This method enables accurate high-Reynolds number flow simulations on a Cartesian grid that is not aligned to the object surface. These simulation methodologies were well validated through the simulations of fundamental flows [14] and the flows around the NASA common research model [11]. The other employed simulation methods are summarized in Table 2.

Table 2 – Simulation methods.				
Turbulence model	SA-noft2 [15]			
Time integration	Matrix-free Gauss–Seidel [16]			
Time stepping	Local time stepping			
Inviscid term	SLAU [17] with fourth-order upwind-biased variable extrapolation [18]			
Viscous term	Second-order central difference [19]			

Table 2 - Simulation methods

2.2 Computational grids

Figure 3 shows the overview of the hierarchical Cartesian grids generated by UTCart. The minimum cell size Δx_{\min} is $1/1024C_{\mathrm{ref}}$ (i.e., 0.27 inch in the full-scale of the CRM), and the cell size on the wing, nacelle, fuselage, and wind tunnel walls are Δx_{\min} , $2\Delta x_{\min}$, $4\Delta x_{\min}$, and $32\Delta x_{\min}$, respectively. The total numbers of cells in the in-tunnel and free-air configurations are approximately 120 million and 75 million, respectively. Note that the total number of cells slightly varies depending on the angle of attack and peniche settings.

In-tunnel configuration

Free-air configuration

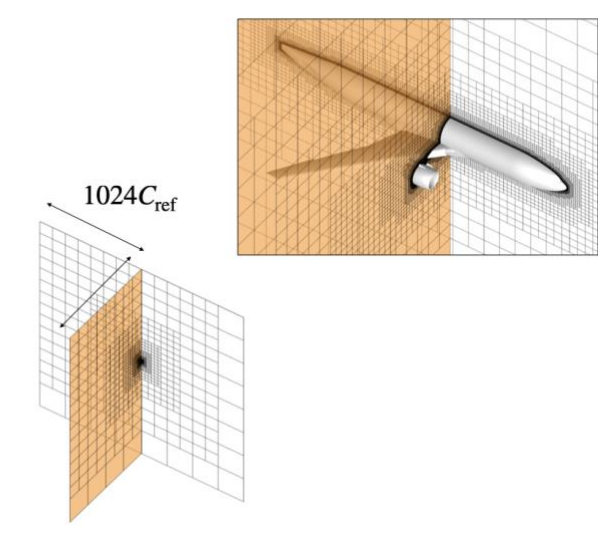


Figure 3 – UTCart-generated hierarchical Cartesian grids around the CRM-HL.

3. Validations

First, the results of FA and 35N are compared to the experimental data [1]. Figure 4 shows the obtained C_D-C_L and $C_L-\alpha$ curves. Note that the force working on the peniche is excluded from the integration of these force coefficients. Here, the results of FA and 35N are compared to the experimental data with and without the wind-tunnel correction, respectively. In $\alpha_c \leq 17.05^\circ$ ($\alpha \leq 15.48^\circ$ in 35N), C_D and C_L of FA and 35N reasonably match the experimental data with and without the wind-tunnel correction, respectively. These results suggest that the wind-tunnel correction (i.e., the difference between the corrected and uncorrected experimental data) is well predicted by the CFD simulation. When looking at the results more closely, the CFD results tend to underestimate C_D and overestimate C_L at $\alpha_c = 2.78^\circ$ and $\alpha_c = 7.05^\circ$. These slight discrepancies may be due to the difference in the flow separation at the flap trailing edge, as described later.

The aerodynamic coefficients at the near-stall conditions of attack show more variation than those at the low angles of attack. In FA, the stall occurs at α_c =21.47°. The stall angle is consistent with the experiment, although C_L decreases too quickly after the stall occurs. In 35N, the stall occurs at α_c =19.57° (α =17.98°), which is slightly earlier than the wind tunnel experiment. The difference between FA and 35N suggests that the stall angle of the semi-span model experiment becomes lower than that of the full-span model experiment, which agrees with the observation by Gatlin and McGhee [3].

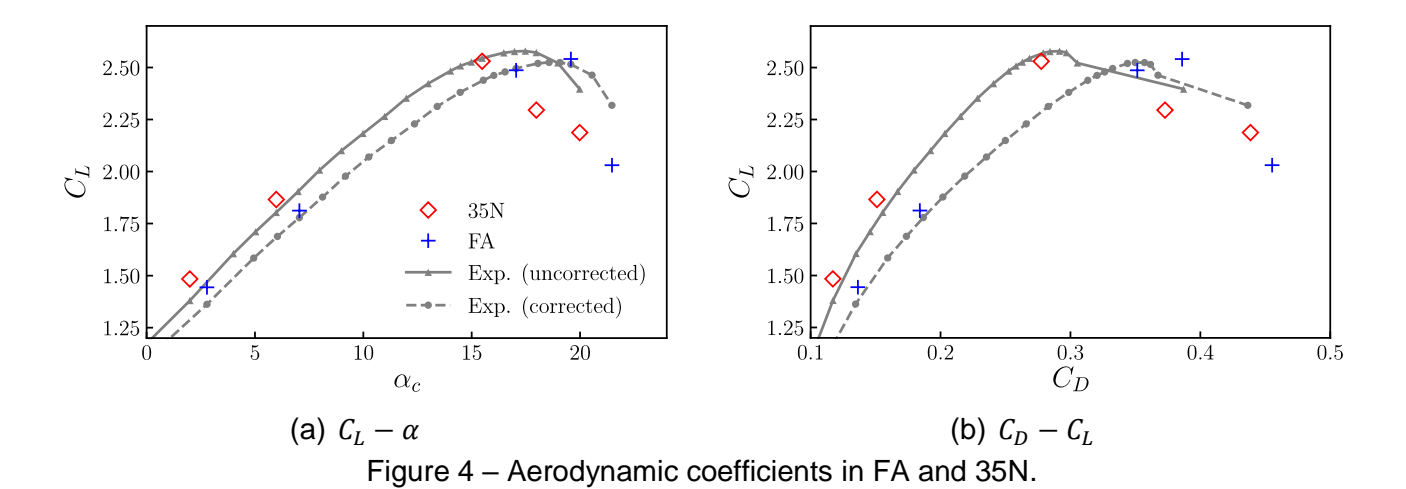


Figure 5 shows surface streamlines at α_c =7.05°, 19.57° and 21.47° over the upper wing surface. At α_c =7.05°, the flow is mostly attached both in FA and 35N. However, the wind tunnel experiment shows notable flow separation over the flap. The difference in the flow separation is essentially the cause of the underestimation of the C_D and the overestimation of C_L at the low angles of attack. At $\alpha_c \geq 19.57^\circ$, flow separation occurs downstream of the slat support in the outboard region. Similar flow separation is observed in the oil-flow visualization shown in Fig. 6, although the size of the separated region tends to be overestimated in the CFD results. Furthermore, the onset angle of wing-root separation differs between FA and 35N. In FA, the separation first occurs at α_c =21.47°, while it occurs at α_c =19.57° in 35N. The onset of the separation corresponds to the stall angles shown in Fig. 4, suggesting that the wing-root separation is the primary cause of the stall.

Figure 7 shows the distributions of the surface pressure coefficient \mathcal{C}_p over spanwise cross-sections at α_c =7.05°, 19.57° and 21.47°. At α_c =7.05°, the obtained \mathcal{C}_p distributions are in reasonable agreement with the wind tunnel experiment. The remaining discrepancy is the distribution near the flap trailing edge at Section E, which is due to the difference in the flow separation near the flap trailing edge (see Figs 5 (a) and 6 (a)). At α_c =19.57°, the suction peak in the inboard region (Section A) is lost in 35N but is retained in FA. This difference corresponds to the difference in the separation (see Fig. 5 (b) and (e)). At α_c =21.47°, the suction peak is lost in both FA and 35N. Also, the suction

peak at Section H is underestimated slightly in both 35N and FA. This difference seems to occur because the CFD simulations overestimate the size of the wing-tip separation.

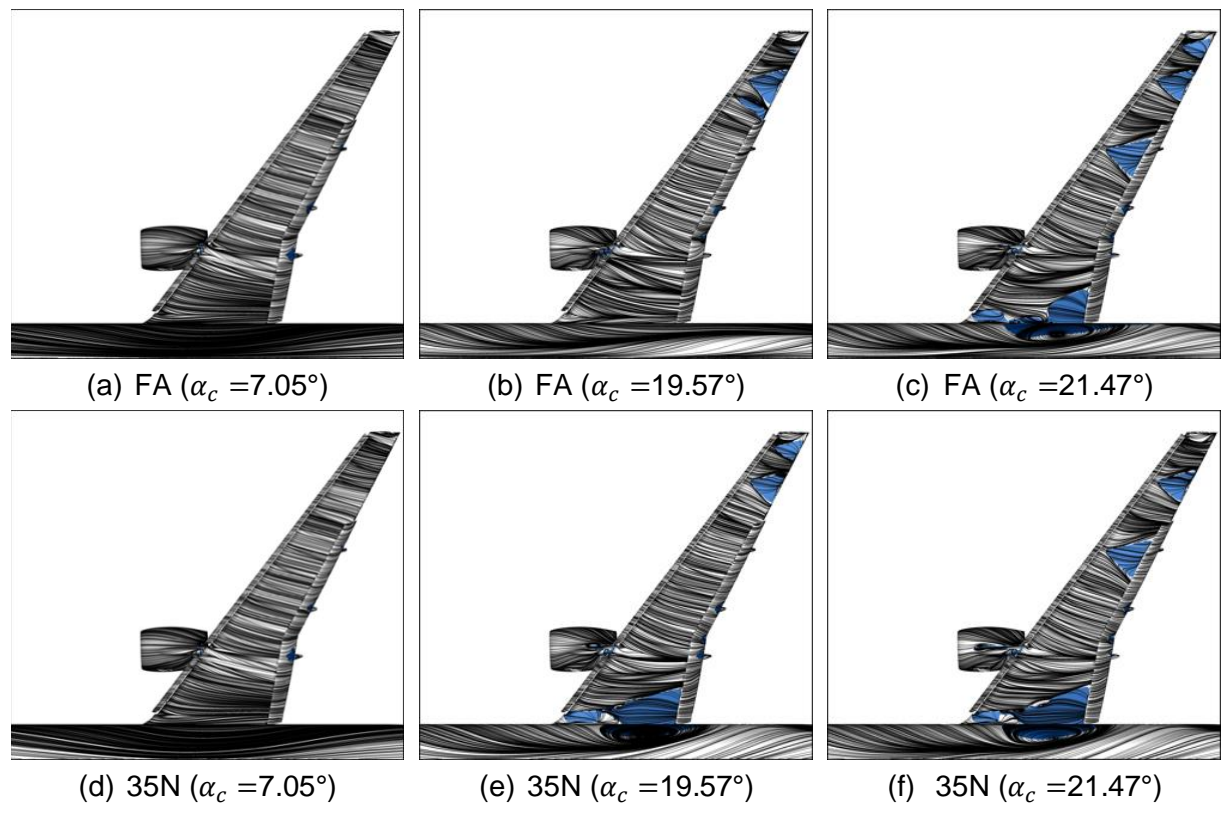


Figure 5 – Surface streamlines. The region $\mathcal{C}_{f,x} < 0$ are shown in blue.

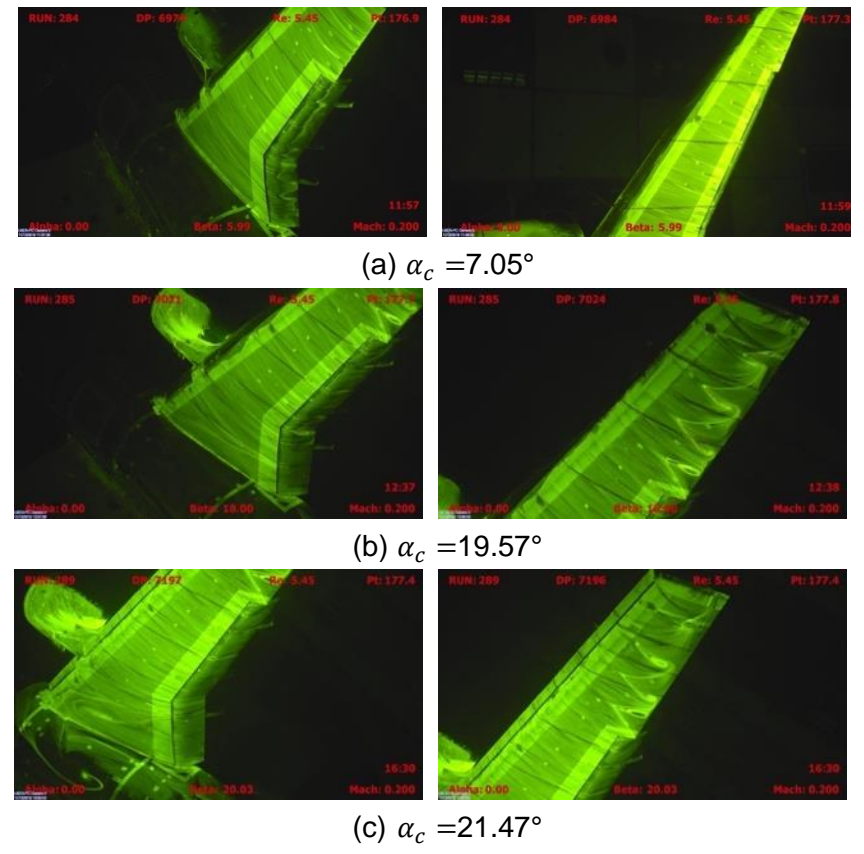


Figure 6 – Oil-flow visualization in the wind tunnel experiment [1] (available at [12]).

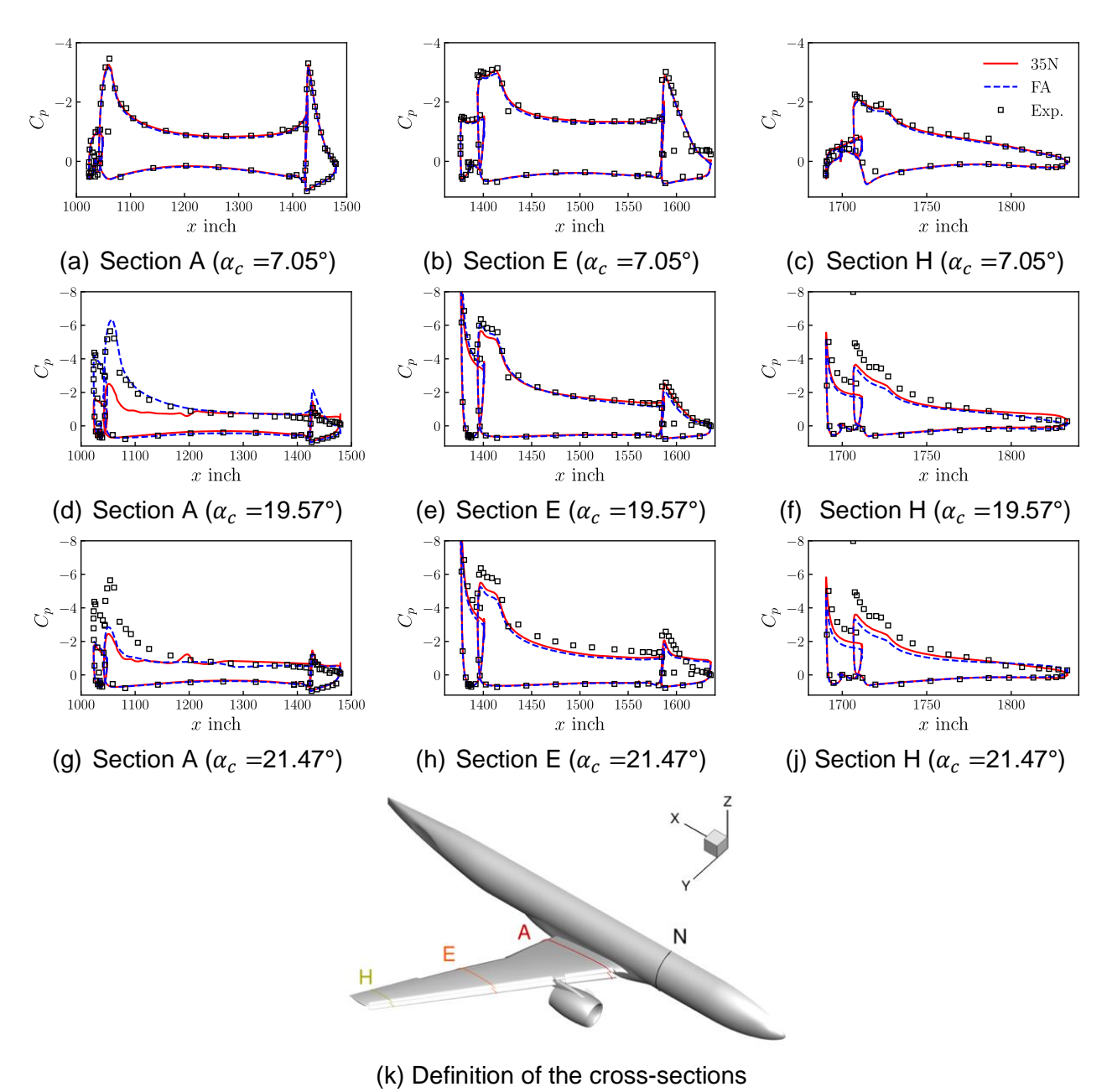


Figure 7 – Surface pressure coefficients over the spanwise cross-sections.

Furthermore, Fig. 8 compares the profiles of the total pressure loss coefficient within the floor boundary layer at an upstream location of the model (x =-54.27 inch, z =-152.2 inch) in 35N. Table 3 summarizes the displacement thickness δ^* , shape factor H, and 99% boundary layer thickness δ_{99} at this location. Note that the result shown here is at α_c =19.57° (α =17.98°), while the results at the other angles of attack are almost the same as the result shown here. The present CFD result significantly underestimates the boundary layer thickness. Also, the shape factor obtained by the present simulation is the typical value for a turbulent boundary layer (1.3~1.4), whereas the value achieved in the wind tunnel experiment is considerably higher. This discrepancy is not unique to the present CFD simulations but is also observed in other CFD simulations of the same wind tunnel [20]. This result suggests that the subscribed boundary condition, e.g., the fully turbulent wall for the wind tunnel floor, is not perfectly compatible with the actual experimental conditions.

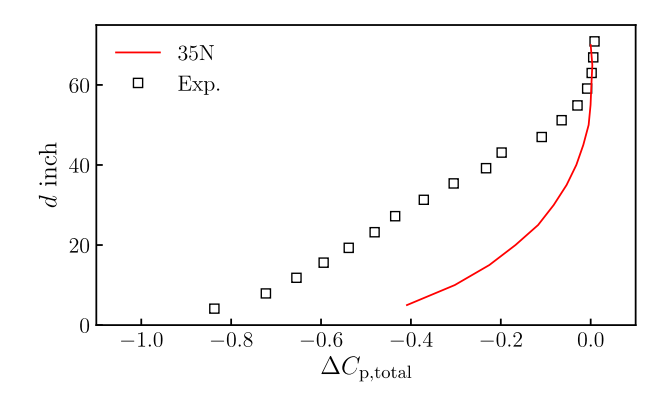


Figure 8 – Wall-normal profile of total pressure loss coefficient upstream of the model in 35N at α_c =19.57°, where d represents the wall distance.

Table 3 – Boundary layer thicknesses upstream of the model.

	UTCart (35N)	Wind tunnel experiment [1]			
Displacement thickness δ^* inch	5.16	15.1			
Shape factor <i>H</i>	1.32	1.71			
99% thickness δ_{99} inch	45.2	56.8			

In summary, the present CFD simulations predict the stall behavior of the wind tunnel experiment qualitatively well, although the quantitative aspects (i.e., the angle of attack and the separation size) are slightly different from the experiment. Note that we have also conducted the same simulation by reducing the grid size and confirmed the aerodynamic coefficients and the separation patterns are almost grid-converged (see Appendix A). Hence, the possible causes for the difference between the CFD and wind tunnel results are the turbulence model and the boundary conditions, including the floor boundary layer thickness. Although further examination of these factors is desirable to pursue quantitative prediction of the stall, in the following, we focus on the difference between the CFD results to clarify the effects of the peniche and floor boundary layer.

4. Effects of peniche and floor boundary layer

As described in Section 3, the stall angle is different between FA and 35N. To clarify the cause of this difference, we investigate the effects of the peniche height and the tunnel wall boundary condition. Figure 9 summarizes the aerodynamic coefficients of 0N, 35N, and 175N. Figure 9 indicates that both stall characteristics and lift slope vary by the peniche height and tunnel wall boundary condition. In the following, we discuss the differences in the stall characteristics and lift slope separately.

4.1 Stall characteristics

Figure 10 shows the surface streamlines at α_c =19.57° (α =17.98°) for each case in Table 3. The surface streamlines in 0S resemble the streamlines in FA, where the wing-root separation does not appear. This result suggests that the inviscid (i.e., potential) effect of the wind tunnel is not the fundamental cause of the difference in the wing-root separation. In contrast to FA and 0S, the wing-root separation is observed in 0N, 35S, and 175N. The difference between 0S and 0N suggests that the floor boundary layer is one of the causes of the wing-root separation, as reported in Ref. [4]. However, 35S and 175N, which essentially avoid the influence of the floor boundary layer, also exhibit flow separation at the wing root.

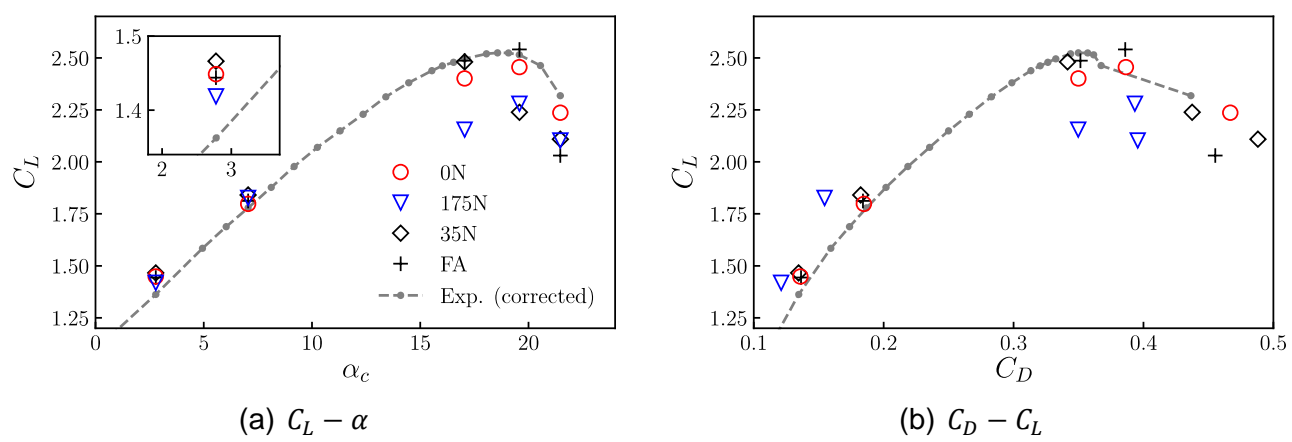


Figure 9 – Effects of the peniche and floor boundary layer on the aerodynamic coefficients. The results with the in-tunnel configurations are corrected using the difference between the uncorrected and corrected wind-tunnel results.

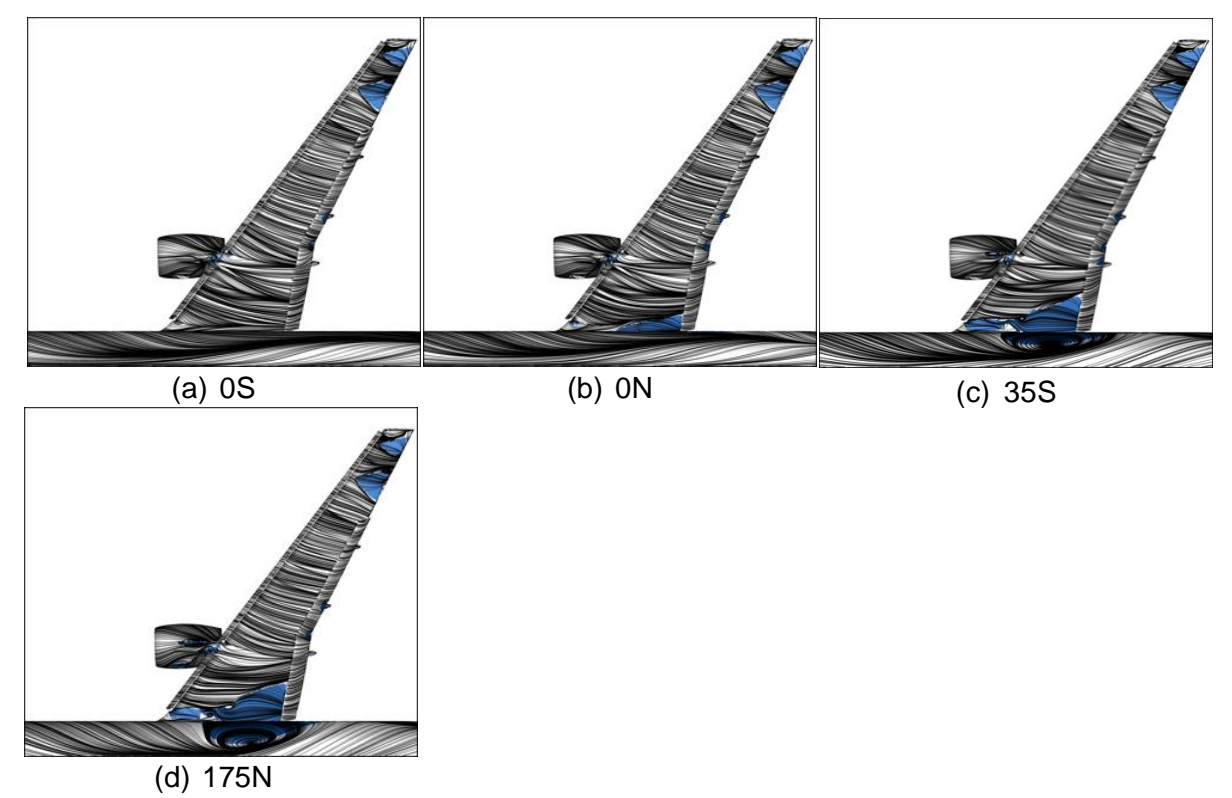


Figure 10 – Surface streamlines (α_c =19.57°, see Fig. 5 for FA and 35N).

Figure 11 shows the distributions of the total pressure coefficient $C_{p,\mathrm{total}}$ near the wing-body junction. Here, only the regions with $C_{p,\mathrm{total}} < -0.2$, i.e., those affected by viscosity are shown. Compared to FA, the boundary layer over the filet (i.e., the fuselage upstream of the wing-body junction) thickens in 0N and 35N. A similar thickening of the boundary layer was reported in Ref. [5], which argues that the entrainment of the floor boundary layer into this region causes the thickened boundary layer. In contrast to 0N and 35N, the boundary layer thickness over the fuselage in 35S and 175N is almost the same as FA. However, the wing-root separation remains in these cases and even enlarges by increasing the peniche height. These results suggest that a high peniche enhances the wing-root separation. Indeed, as shown in Fig. 9, the stall angle decreases as the peniche height increases. To further clarify the aerodynamic effects of the peniche, we investigate the differences in the surface C_p distribution at $\alpha_c = 7.05^{\circ}$ ($\alpha = 5.98^{\circ}$), where the difference in the flow separation is minor. Figure 12 shows the difference in C_p between FA and each in-tunnel case. Here, the suction near the wing

EVALUATING INSTALLATION EFFECTS IN SEMI-SPAN WIND TUNNEL EXPERIMENTS USING UTCART

leading edge strengthens as the peniche height increases. The difference in \mathcal{C}_p is more noticeable in the inboard region. Reference [3] also reported a similar augmentation of the suction in the inboard section. The cause of this augmentation may be explained by the flow around the fuselage shown in Fig. 13. This figure visualizes the distributions of the cross-sectional (i.e., vertical to the fuselage axis) velocity over the axial cross-plane upstream of the wing-body junction (section N in Figure 7 (k)). The flow around the fuselage strengthens when increasing the peniche height. This upward flow increases the effective angle of attack of the inboard wing. The increase in the effective angle of attack causes a stronger adverse pressure gradient over the upper wing surface, making the inboard region prone to separation. Therefore, these results suggest that the peniche height may also be the factor for the stall.

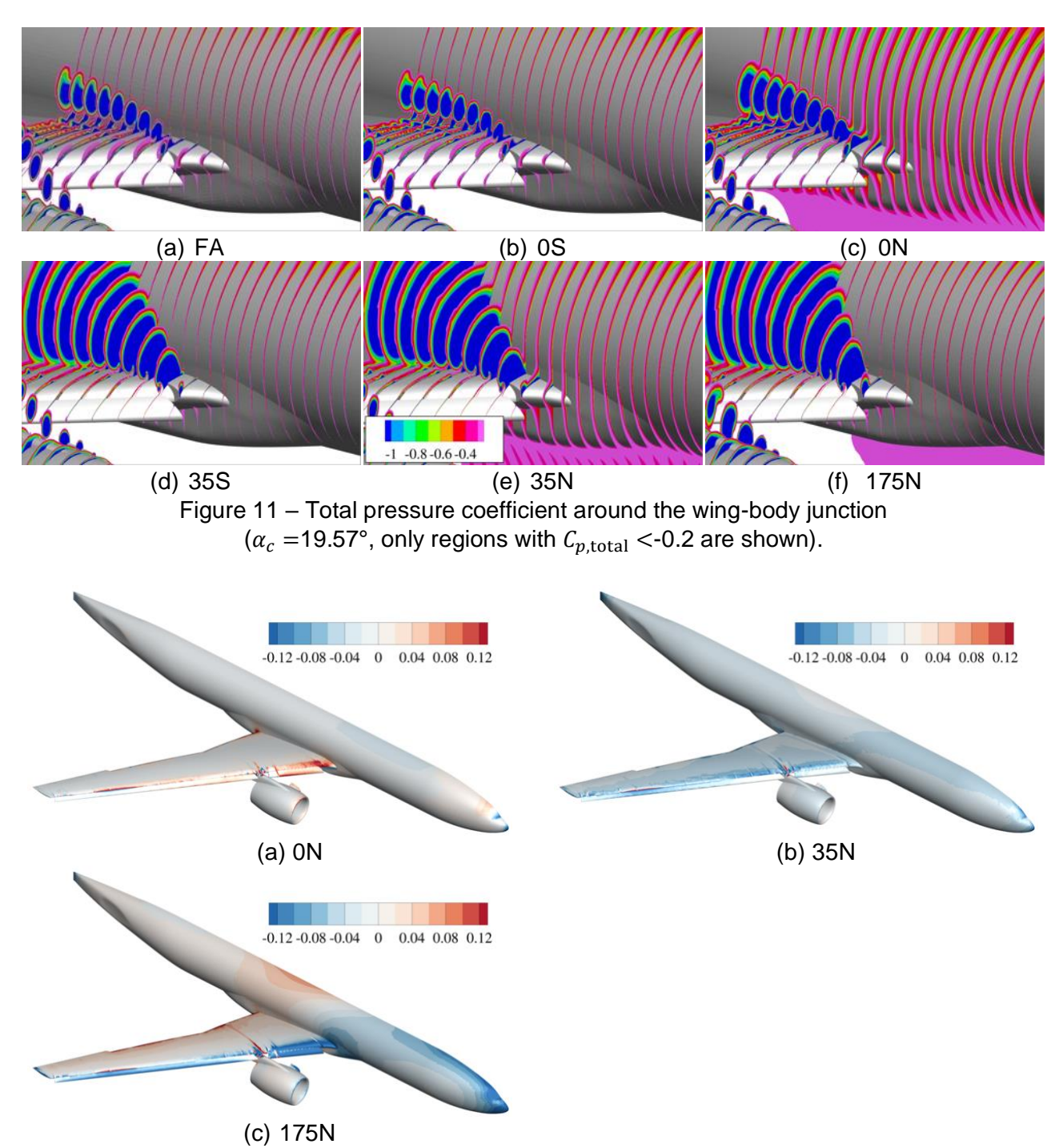


Figure 12 – Difference in the surface pressure coefficient compared to FA (α_c =7.05°).

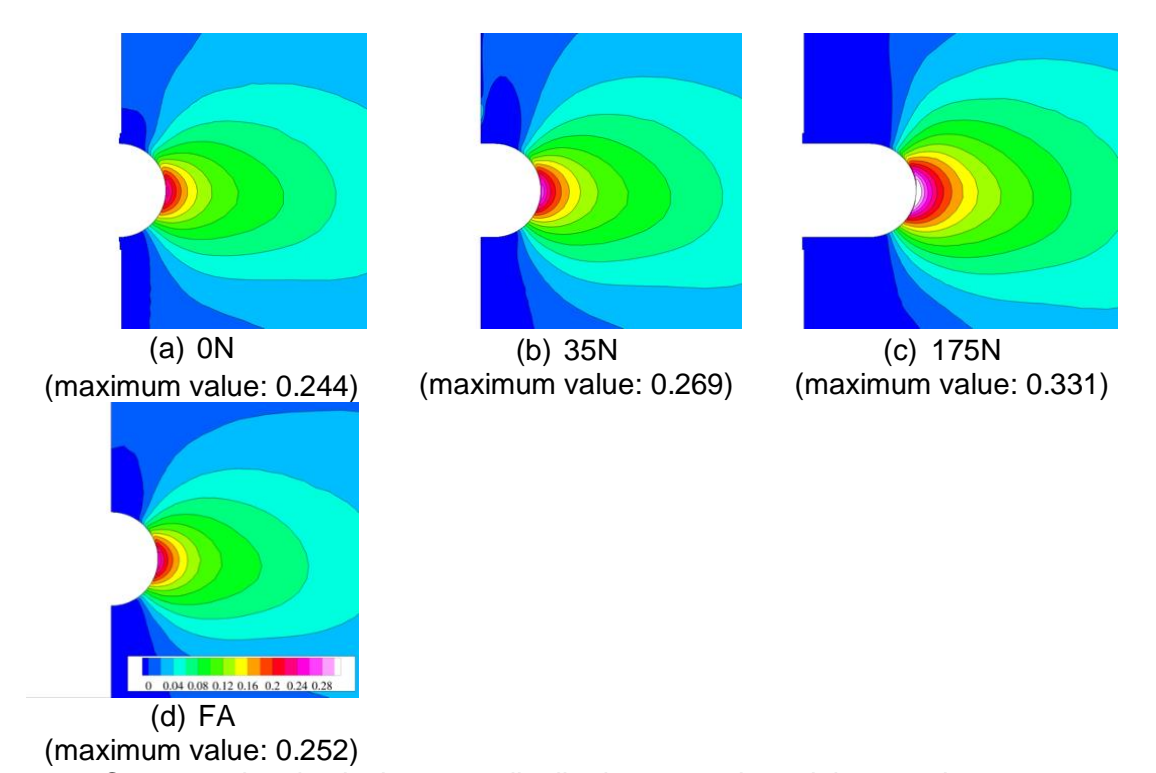


Figure 13 – Cross-sectional velocity w/u_{∞} distributions over the axial cross plane upstream of the wing-body junction (α_c =7.05°).

4.2 Lift slope

Table 4 summarizes the lift slope between α_c =2.78° and 7.05°. The lift slope increases as the peniche height increases, while the behavior of the lift coefficient itself is not monotonic with respect to the peniche height (see Fig. 9 (a)). The increase in the lift slope agrees with the previous studies [3, 4]. Note that all the simulation results in this study consistently underestimate the lift slope compared to the experimental data. The difference between the simulation and wind tunnel experiment may be due to the difference in the flow separation near the flap trailing edge, as discussed in Section 3.

Table 4 –Effects of the peniche height on the C_L slopes between α_c =2.78° and 7.05°.

Case	0N	35N	175N	FA	Exp. (corrected)
Slope rad ⁻¹	4.690	5.028	5.472	4.941	5.586

5. Effects of the gap between the floor and model

Next, the effects of the gap (35N-g1 and 35N-g2, see Fig. 2) are investigated. Figure 14 compares the aerodynamic coefficients of 35N, 35N-g1, and 35N-g2. At the low angles of attack, the gap increases the drag and decreases the lift. These results reconfirm the observation by Skinner and Zare-Behtash [7]. Since 35N-g1 has a wider gap compared to 35N-g2, the influence of the gap becomes more noticeable. Also, Table 5 summarizes the lift slope between α_c =2.78° and 7.05°. The lift slope decreases as the gap enlarges. Here, 35N-g2 shows the best agreement with the FA configuration within the cases simulated in this study. Also, Figure 15 shows the C_p difference to FA. The gap tends to increase C_p in the inboard region, i.e., decrease the effective angle of attack. This effect is opposite to the peniche discussed in Section 4. The cause of the decrease in the angle of attack can also be explained by the cross-sectional velocity distribution shown in Fig. 16. As in these figures, the upward flow around the fuselage decreases as the gap becomes large. Reference [7] explains this phenomenon from the circulation around the fuselage. Namely, the upward flow in the gap causes circulation around the fuselage and reduces the lift produced by the fuselage.

At the high angles of attack, the stall angle increases by the gap. Figure 17 shows the surface

EVALUATING INSTALLATION EFFECTS IN SEMI-SPAN WIND TUNNEL EXPERIMENTS USING UTCART

streamlines at α_c =19.57° and 21.47°. The wing-root separation does not occur even at α_c =21.47° in 35N-g1, while it occurs between α_c =19.57° and 21.47° in 35N-g2. Therefore, the stall behavior of 35N-g2 resembles that of FA. Also, Figure 18 shows the distribution of the total pressure coefficient $C_{p,\text{total}}$ around the wing-body junction. The boundary layer thicknesses over the upstream fuselage in 35N-g1 and 35N-g2 are thinner than 35N and almost similar to FA (see Fig. 11 (a) and (e)). These results suggest that the gap is also effective in avoiding the unfavorable effects of the floor boundary layer.

In summary, the gap has the effect opposite to the peniche, i.e., it reduces the effective angle of attack in the inboard region. This effect inhibits the wing-root separation at the high angle of attack. The gap also reduces the influence of the floor boundary layer. Hence, by appropriately designing the peniche with a gap (or holes through the peniche), the aerodynamics of the semi-span model may become comparable to that of the full-span model. Therefore, the present 35N-g2 configuration is assumed to be the best compromise for simulating the full-span model aerodynamics using a half-span model.

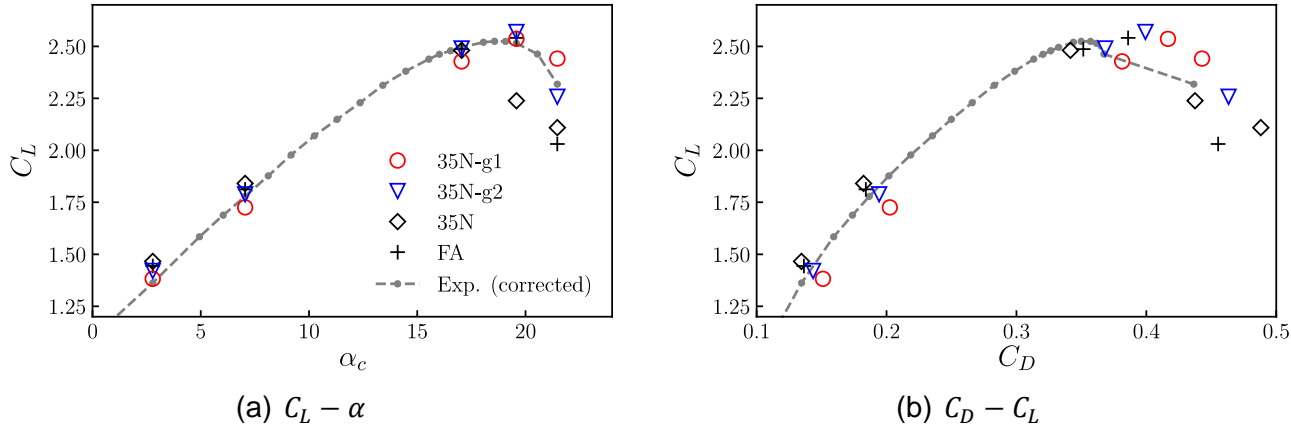


Figure 14 – Effects of the gap on the aerodynamic coefficients. The results with the in-tunnel configurations are corrected using the difference between the uncorrected and corrected wind-tunnel results.

Table 5 – Effects of the gap on the C_I slopes between $\alpha_c = 2.78^{\circ}$ and 7.05°.

		3-1	- L I		
Case	35N-g1	35N-g2	35N	FA	Exp. (corrected)
Slope rad ⁻¹	4.607	4.949	5.028	4.941	5.586

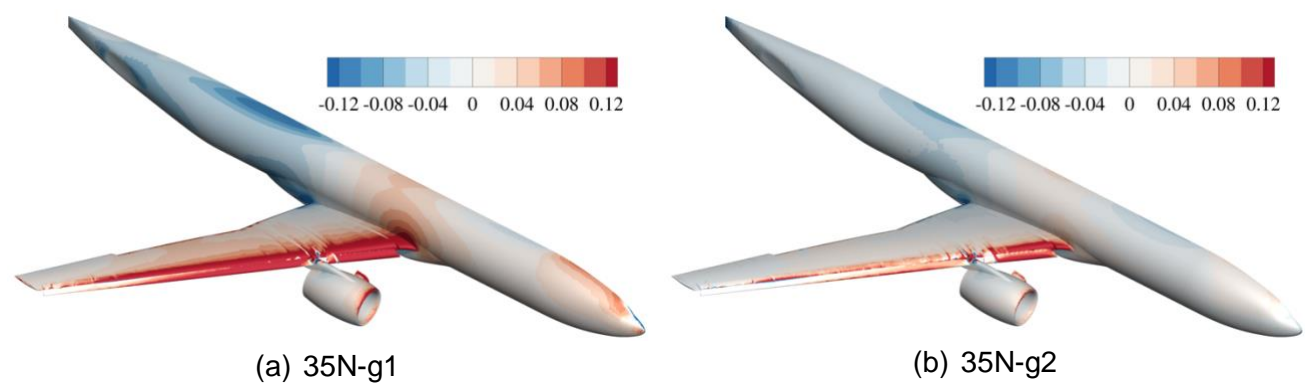


Figure 15 – Effects of the gap on the surface pressure coefficient (α_c =7.05°, showing difference to FA).

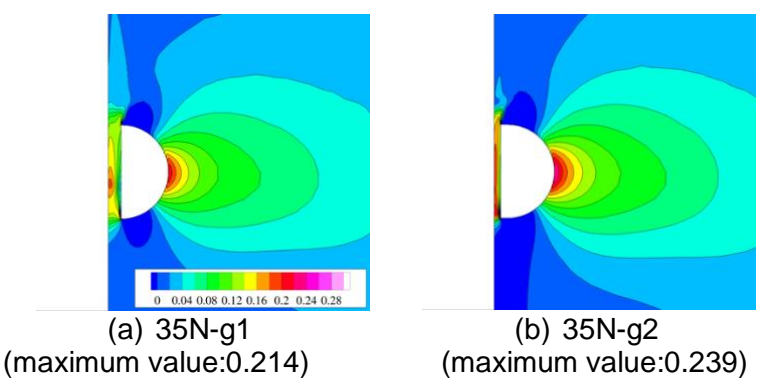


Figure 16 – Cross-sectional velocity w/u_{∞} distributions over the axial cross-plane upstream of the wing-body junction ($\alpha_c = 7.05^{\circ}$).

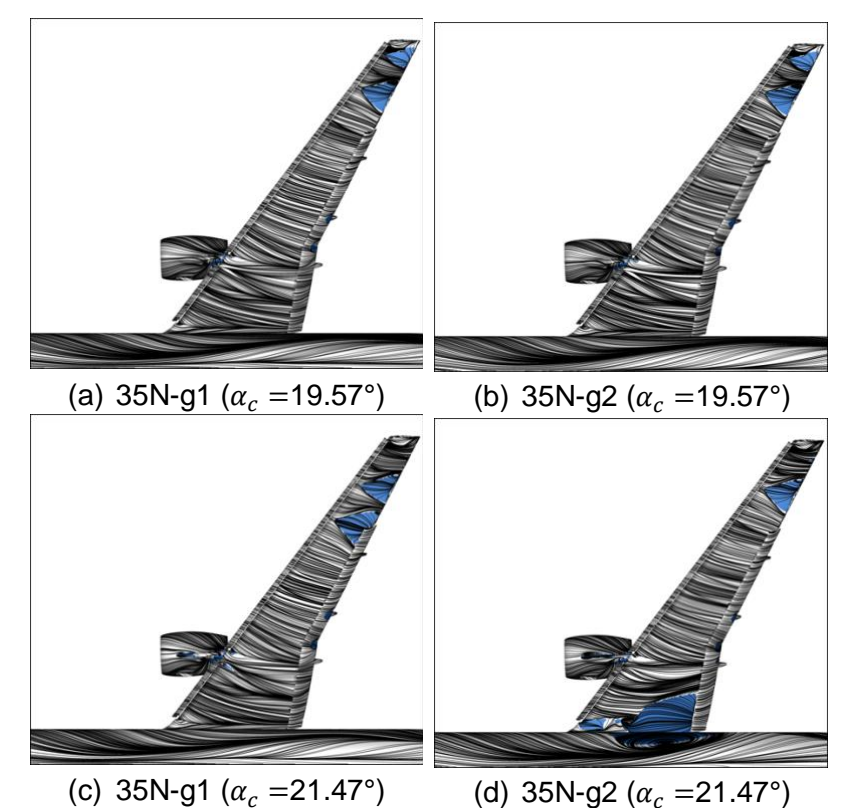


Figure 17 – Effects of the gap on surface streamlines (see Fig. 5 and 10 for the other cases).

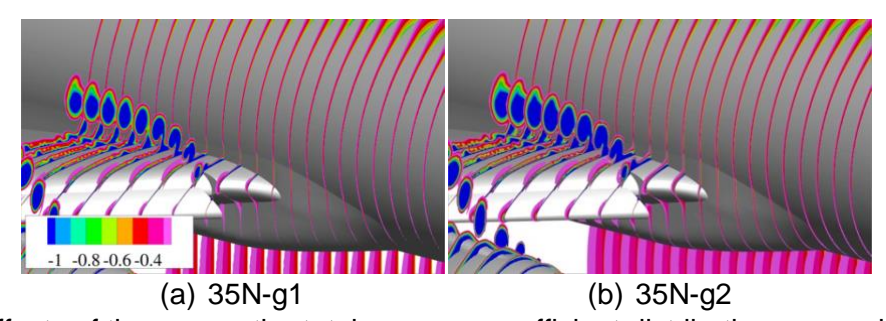


Figure 18 – Effects of the gap on the total pressure coefficient distributions around the wing-body junction (α_c =19.57°, only $C_{p,\text{total}} < -0.2$ is visualized. See Fig. 11 for the other cases).

6. Conclusions

The model installation effects in the semi-span model wind tunnel experiment of the CRM-HL were investigated through RANS-based CFD simulations using the Cartesian-grid-based flow solver UTCart. UTCart enables fully automatic grid generation and realizes rapid turn-around time for flow

simulations around various complex geometries. Using UTCart, we conducted in-tunnel flow simulations with changing the peniche geometries. Moreover, we also investigated the effects of the floor boundary layer by switching the boundary condition for the tunnel wall from nonslip to slip conditions.

The simulation results reconfirmed that the floor boundary layer thickens the boundary layer over the fuselage and promotes wing-root separation. Such thickening is significant when the peniche height is low. The results also suggested that the peniche increases the effective angles of attack at the inboard sections. Hence, the flow separation tends to occur from the leading edge of the inboard wing when the peniche height is too high. Furthermore, the gap between the floor and the model decreases effective angles of attack at the inboard sections. The gap also reduces the interaction with the floor boundary layer compared to the peniche with the same height. Therefore, a proper combination of the peniche and the gap may be suitable for imitating the full-span model aerodynamics in the semi-span model wind tunnel experiment.

Appendix A. Grid sensitivity study

To validate the resolution of the employed grid, we also conduct the simulations with the free-air configuration on a finer grid (Grid 2). The minimum cell size of Grid 2 is reduced to 3/4 of the baseline grid (Grid 1), resulting in a total cell number of 157 million.

Figure A1 compares the obtained $\mathcal{C}_D - \mathcal{C}_L$ curves. The aerodynamic coefficients almost do not change between the two grids. Moreover, Fig. A2 shows the surface streamlines on Grid 2. Compared to the results on Grid 1 (Fig. 5 (a-c)), a similar wing-root separation occurs first at α_c =21.47°, although minor differences in the location of the separation downstream of the slat support in the outboard region remain. The location of the outboard flow separations is difficult to predict by the steady RANS simulation because the separation at one location causes loss of the local lift and inhibits the separation at the other location. Therefore, the separation pattern changes by where the separation first occurs, i.e., the results may be dependent on the convergence history. Indeed, the previous study [21] showed that the location of the outboard separations easily changes by the initial condition. Except for this point, the obtained results are almost grid converged and show the validity of the baseline grid used throughout Sections 3 to 5.

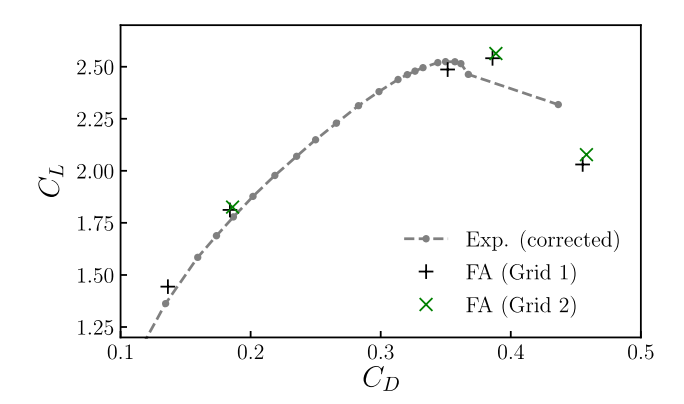


Figure A1 Grid sensitivity on the $C_D - C_L$ curve.

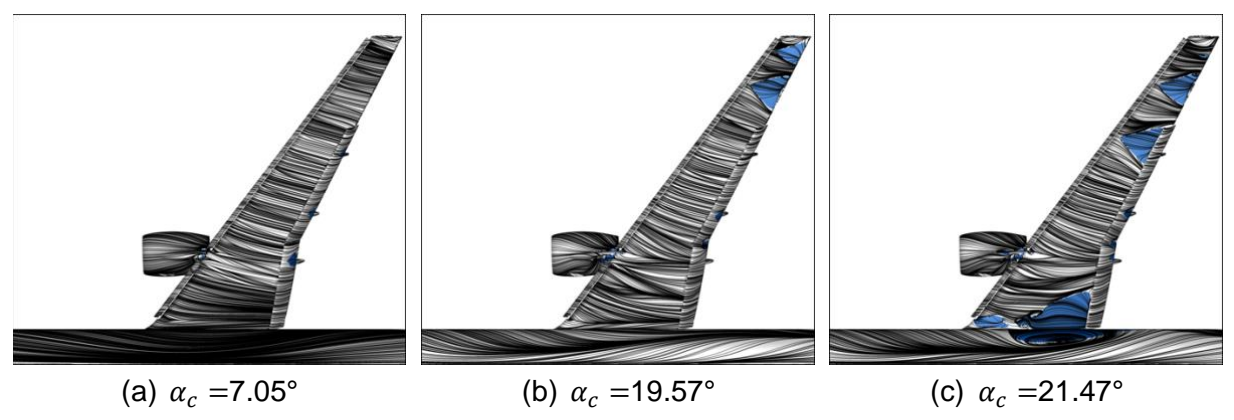


Figure A2 – Surface streamlines (FA on Grid 2).

Acknowledgment

This work is supported by JSPS KAKEHI (21H01527). The computations were conducted on the FUJITSU Supercomputer PRIMEHPC FX1000 and FUJITSU Server PRIMERGY GX2570 (Wisteria/BDEC-01) at the Information Technology Center, The University of Tokyo.

Contact Author Email Address

mailto: ytamaki@g.ecc.u-tokyo.ac.jp

Copyright Statement

The authors confirm that they, and/or their company or organization, hold copyright on all of the original material included in this paper. The authors also confirm that they have obtained permission, from the copyright holder of any third party material included in this paper, to publish it as part of their paper. The authors confirm that they give permission, or have obtained permission from the copyright holder of this paper, for the publication and distribution of this paper as part of the ICAS proceedings or as individual off-prints from the proceedings.

References

- [1] Evans A N, *et al.* Test summary of the NASA high-lift common research model half-span at QinetiQ 5-metre pressurized low-speed wind tunnel. *AIAA Aviation 2020 Forum*, online, AIAA 2020-2770, 2020.
- [2] Yokokawa Y, *et al.* Investigation and improvement of high-lift aerodynamic performances in lowspeed wind tunnel testing. *46th AIAA Aerospace Sciences Meeting and Exhibit*, Reno, AIAA 2008-0350, 2008.
- [3] Gatlin G M and McGhee R J. Study of semi-span model techniques. *14th Applied Aerodynamics Conference*, New Orleans, AIAA 96-2386, 1996.
- [4] Yokokawa Y, et al. Aerodynamic influence of a half-span model installation for high-lift configuration experiment. 48th AIAA Aerospace Sciences Meeting Including the New Horizons Forum and Aerospace Exposition, Orlando, AIAA 2010-0684, 2010.
- [5] Ito Y, et al. Wind tunnel installation effects on Japan Aerospace Exploration Agency's standard model. *Journal of Aircraft*, Vol. 59, No. 5, pp. 1281-1302, 2022.
- [6] Eder S, Hufnagel K and Tropea S. Semi-span testing in wind tunnels. 25th International Congress of the Aeronautical Sciences, Hamburg, 2006.
- [7] Skinner S N and Zare-Behtash H. Semi-span wind tunnel testing without conventional peniche. *Experiments in Fluids*, Vol. 58, pp. 1-18, 2017.
- [8] Malik A and Render P M. Use of wall suction in half model wind tunnel testing. 28th AIAA Applied Aerodynamics Conference, Chicago, AIAA 2010-4828, 2010.
- [9] Mamou M and Broughton C A. Investigation of aerodynamic support interference for testing a semispan T tail aircraft model. *Journal of Aircraft* Vol. 60, No. 3, pp. 915-934, 2023.
- [10] Imamura T, Tamaki Y and Harada M. Parallelization of a compressible flow solver (UTCart) on cell-based refinement Cartesian grid with immersed boundary method, *Proceedings of the 29th International Conference on Parallel Computational Fluid Dynamics*, Glasgow, 2017.
- [11] Tamaki Y and Imamura T, Turbulent flow simulations of the common research model using immersed boundary

EVALUATING INSTALLATION EFFECTS IN SEMI-SPAN WIND TUNNEL EXPERIMENTS USING UTCART

method, AIAA Journal, Vol. 56, No. 6, pp. 2271-2282, 2018.

- [12] https://hiliftpw.larc.nasa.gov/index-workshop4.html (retrieved on Apr. 8th, 2024).
- [13] Rumsey C L, Slotnick J P and Woeber C D. Fourth high-lift prediction/third geometry and mesh generation workshops: Overview and summary. *Journal of Aircraft* Vol. 60, No. 4, pp. 1160-1177, 2023.
- [14] Tamaki Y, Harada M and Imamura T. Near-wall modification of Spalart–Allmaras turbulence model for immersed boundary method, *AIAA Journal*, Vol. 55, No. 9, pp. 3027-3039, 2017.
- [15] https://turbmodels.larc.nasa.gov/spalart.html (retrieved on Apr. 8th, 2024).
- [16] Shima E. A Simple implicit scheme for structured/unstructured CFD. 29th Fluid Dynamics Symposium, Japan Soc. for Aeronautical and Space Sciences, Sapporo, Paper 2C9, 1997 (in Japanese).
- [17] Shima E and Kitamura K. Parameter-free simple low-dissipation AUSM-family scheme for all speeds. *AIAA Journal* Vol. 49, No. 8, pp. 1693-1709, 2011.
- [18] Tamaki Y and Imamura T. Efficient dimension-by-dimension higher order finite-volume methods for a Cartesian grid with cell-based refinement. *Computers & Fluids*, Vol. 144, pp. 74-85, 2017.
- [19] Wang G, Schwöppe A and Heinrich R. Comparison and evaluation of cell-centered and cell-vertex discretization in the unstructured tau-code for turbulent viscous flows. *ECCOMAS CFD2010*, Lisbon, 2010.
- [20] Kiris C, et al. High-lift common research model: RANS, HRLES, and WMLES perspectives for CLmax prediction using LAVA. AIAA SciTech 2022 Forum, San Diego, AIAA 2022-1554, 2022.
- [21] Ollivier-Gooch C F and Coder, J G. Lessons learned by the fixed-grid RANS TFG for HLPW-4/GMGW-3. *AIAA Aviation 2022 Forum*, Chicago, AIAA 2022-3211, 2022.